Supplementary Information

Dual Single-Atom Sites Coupled with Graphene-Encapsulated Core-Shell Fe-Cu Nanoalloy for Boosting Oxygen Reduction Reaction

Katam Srinivas[a1], Zhuo Chen[b,1], Anran Chen[c], He Huang[a], Chengtao Yang[a], Fei Wang[d,e*], Ming-qiang Zhu[b*], and Yuanfu Chen[a*]

[a] School Yangtze Delta Region Institute (Huzhou), and School of Integrated Circuit Science and Engineering, University of Electronic Science and Technology of China, 313001 Huzhou, Zhejiang, PR China

[b] College of Mechanical and Electronic Engineering, Northwest A&F University, Yangling, 712100, PR China

[c] School of Materials and Energy, Yunnan University, Kunming 650091, PR China

[d] Faculty of Materials Science and Engineering, Kunming University of Science and Technology, Kunming 650093, PR China

[e] College of Materials Science and Engineering, Sichuan University, Chengdu 610065, PR China

* Corresponding authors.

E-mail addresses: echo1994wf@foxmail.com (F. Wang), zmqsx@nwsuaf.edu.cn (M.-q. Zhu), yfchen@uestc.edu.cn (Y. Chen).

[1] These authors contributed equally to this work.

1. Experimental Section

Absolute ethanol and the distilled water were used in washing the materials throughout the investigations.

1.1 Structural characterizations

Scanning electron microscope (SEM) images were carried out on a ZEISS Gemini 300. Transmission electron microscopy (TEM), high-resolution TEM (HR-TEM), high angle annular dark field scanning transmission electron microscopy (HAADF-STEM), and element mapping analysis images were examined on a Talos F200X G2 with superX spectroscopy equipment. Aberration-corrected HAADF-STEM (AC-HAADF-STEM) images were carried out on FEI-Themis Z. X-ray diffraction (XRD) data were tested on a Rigaku Smartlab. Raman spectra data were measured on a Renishaw confocal microscope. X-ray photoelectron spectroscopy (XPS) data were obtained on a Thermo Scientific K-Alpha. N_2 adsorption/desorption isotherms (NADI) were obtained on a Micromeritics ASAP 2460 at 77 K. Inductively coupled plasma optical emission spectroscopy (ICP-OES) results were gained on a PE Avio 200.

1.2 Electrochemical characterizations

Electrochemical **ORR** measurements were carried out in O_2- and N_2-saturated 0.1 M KOH by using an electrochemical workstation (Pine, WaveDriver20) equipped with three electrodes. Wherein the catalyst-loaded rotating disc electrode (RDE, Pine, 5 mm; for CV, LSV, CSCA, CV cycling, *i-t*, and methanol poisoning) and a rotating-ring disc electrode (RRDE, Pine, N = 0.37; for electron transfer number and H_2O_2 yield) were used as working

electrodes, while the Hg/HgO electrode and Pt wire were used as the reference and counter electrodes, respectively.

Working electrodes were prepared by sonicating 5 mg of catalyst powder in 1 mL of mixed solvents (V_{water} : $V_{ethanol}$ = 3: 1) for 5 minutes. To which, 50 µL of Nafion ink was injected and ultrasonicated for an additional 30 min. Afterwards, 15 µL of catalyst ink was loaded on RDE and RRDE. The loading amounts of all the catalysts, including 20 wt.% Pt/C for ORR, were 0.29 mg cm^{-2}. All measured potentials were corrected versus the reversible hydrogen electrode (RHE) using the Nernst equation (E_{RHE} = $E_{(Hg/HgO)}$ + 0.0591 × pH + 0.098). The cyclic voltammetry (CV) curves were detected from 0.2 to 1.0 V on RDE (50 mV s^{-1}). The linear sweep voltammetry (LSV) curves were investigated from 0.2 to 1.1 V (10 mV s^{-1}, 400-2500 rpm). Cyclic step chronoamperometry (CSCA) was conducted to measure the solution resistance by adding an instantaneous 50 mV step potential at 8 ms. The final LSV data was obtained by subtracting the background current measured in N_2-saturated electrolyte and performing *iR* compensation using the CSCA results. The CV cycling tests were carried out from 0.6 to 1.0 V for continuous 3,000 cycles (200 mV s^{-1}). The long-term durability experiments were executed by a chronoamperometry test on RDE at 0.6 V for 27,000 s (at 1600 rpm). Methanol tolerance tests were carried out by adding 20 mL of methanol to 80 mL of 0.1 M KOH electrolyte.

The Koutecky–Levich equation was provided to evaluate the values of electron transfer number (n).

$$\frac{1}{j} = \frac{1}{j_d} + \frac{1}{j_k} = \frac{1}{B\omega^{1/2}} + \frac{1}{j_k}$$

$$B = 0.2nFC_0D^{2/3}V^{-1/6}$$

Wherein, j: measured current density; j_k: kinetic current density; j_d: diffusion-limited current density; ω: the angular velocity of the disk (rad s^{-1}); F: Faraday constant (96485 C mol^{-1}); C_0: bulk concentration of O_2 (1.2×10^{-6} mol cm^{-3}); D_0: diffusion coefficient of O_2 in 0.1 M KOH (1.9×10^{-5} cm^2 s^{-1}); V: kinematic viscosity of the electrolyte (0.01 cm^2 s^{-1}).

The H_2O_2 yield and 'n' were further detected on RRDE. The LSV was obtained from 1.1 to 0.1 V (5 mV s^{-1}, 1600 rpm). And its ring potential was set at 1.3 V. Used the subsequent equations to calculate their specific values:

$$H_2O_2(\%) = 200 \times \frac{\dfrac{I_r}{N}}{I_d + \dfrac{I_r}{N}}$$

$$n = 4 \times \frac{I_d}{I_d + \dfrac{I_r}{N}}$$

Wherein, I_r: ring current; I_d: disk current; N: collection efficiency of the Pt ring (N = 0.37).

A rechargeable **Zn-Air battery** was constructed in a 6 M KOH aqueous electrolyte consisting of 0.2 M $Zn(Ac)_2$ using a CHI 660D electrochemical workstation. Polished zinc sheet was used as a metal anode (thickness of 0.3 mm), and the FeCu-DSAs@CNT-loaded carbon paper was employed as air cathode. Electrocatalyst ink preparation is the same as above, and the obtained homogeneous link was loaded on carbon paper (1.0 mg cm^{-2}), and dried in a 50 °C electric oven before assembling the Zn-air battery. While Pt/C-ink was also prepared in the same method. Electrolyte was replaced by pausing the experiment in order to check the rechargeability of a ZAB during the charge-discharge cycling test. All the electrochemical data of the as-prepared electrocatalysts presented in this article has been tested twice to make sure all the results are reliable and reproducible.

1.3 DFT methodology

Density functional theory (DFT) calculations were performed using the CASTEP code in Materials Studio 2020.[1] The generalized gradient approximation (GGA) was used in the scheme of Perdew-Burke-Ernzerhof (PBE) to describe the exchange-correlation functional. The cut-off energy for plane wave was set to 500 eV. The energy criterion was set to 10-5 eV in iterative solution of the Kohn-Sham equation. All the structures were relaxed until the residual forces on the atoms declined to less than 0.03 eV/Å. To prevent interaction between periodic units in the vertical direction, a vacuum space of 10 Å was employed. A Monkhorst–Pack scheme with a k-points mesh of 4 × 4 × 3 was used.

The change of free energy (ΔG) is related to energy variation from the initial to final states and is described as the following expression:[2,3]

$$\Delta G = \Delta E + \Delta ZPE - T\Delta S$$

Here, ΔE presents the adsorption energy relating to materials absorbed on surface. ΔZPE, the differences of zero-point energies, and ΔS, the entropy change were both calculated through the vibrational frequencies of adsorbed species. The ΔE was determined as follows:

$$\Delta E = E_{slab + ads} - (E_{slab} + E_{ads})$$

where $E_{slab+ads}$ represent the total energy of the absorbed system, E_{slab} is the energy of clean surface, and E_{ads} is the energy of adsorbate.
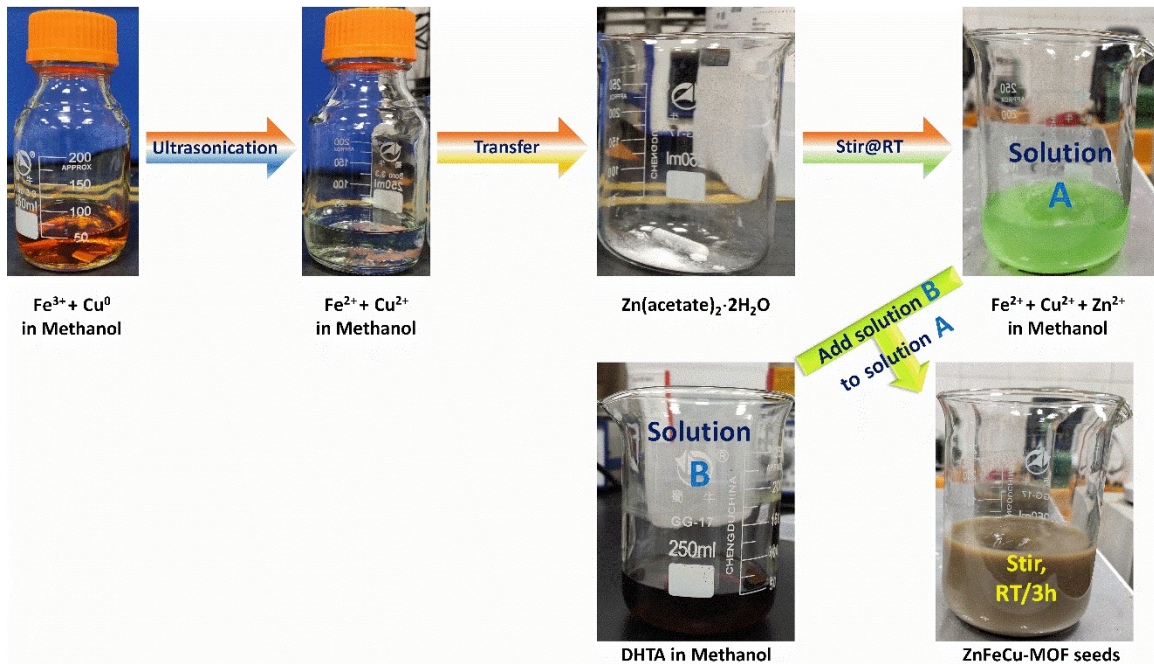
Fig. S1 Photographic representation of ZnFeCu-MOF-74 synthesis strategy.
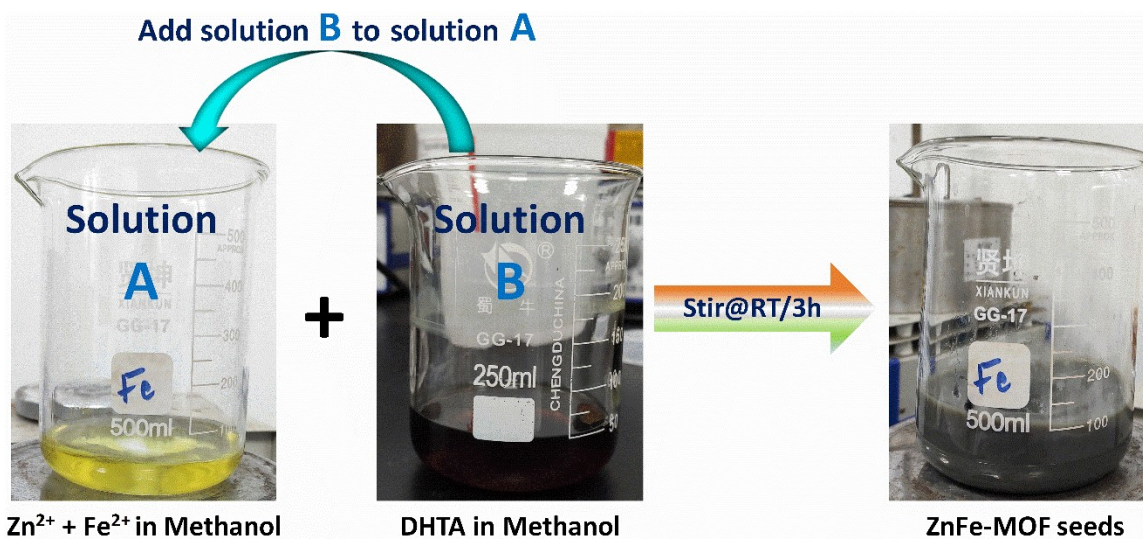
Fig. S2 Photographic representation of ZnFe-MOF-74 synthesis strategy.
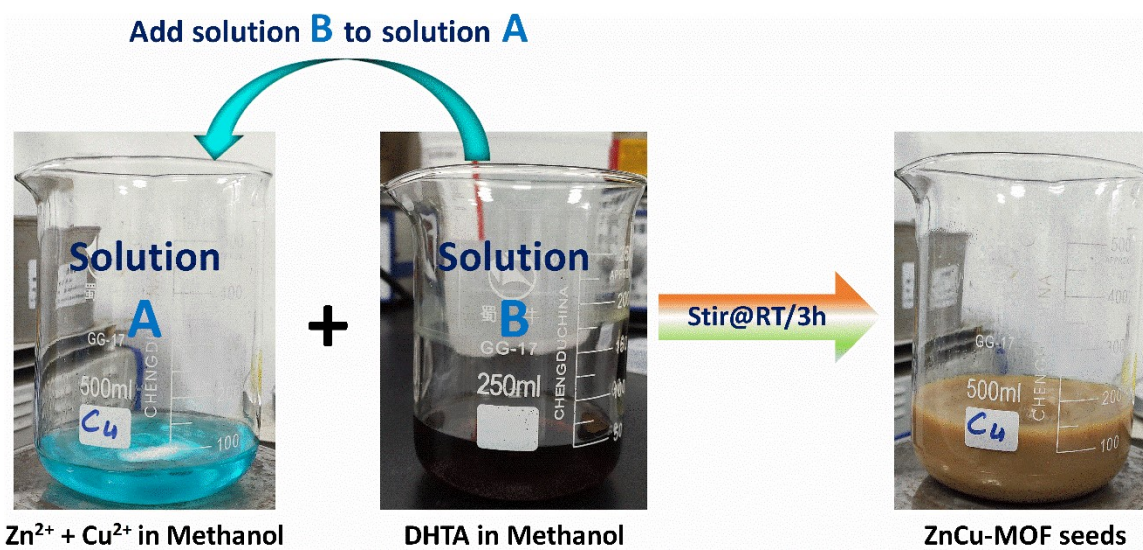
Fig. S3 Photographic representation of ZnCu-MOF-74 synthesis strategy.
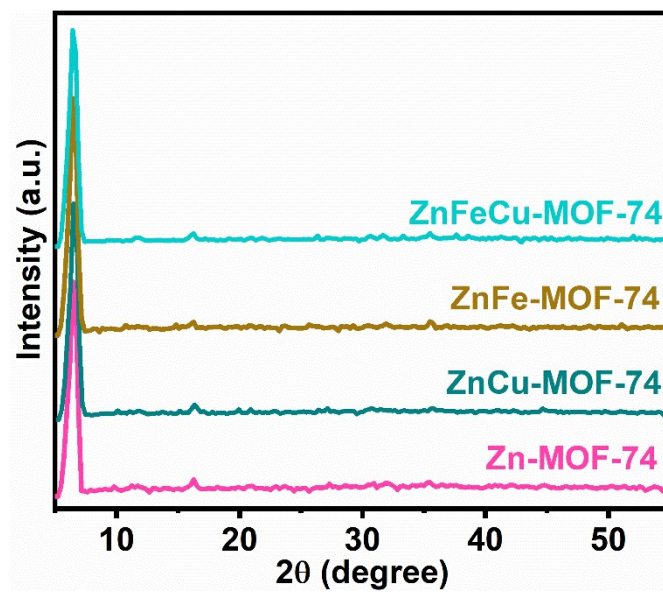
Fig. S4 Powder XRD patterns of Zn-MOF-74, ZnCu-MOF-74, ZnFe-MOF-74 and ZnCu-MOF-74.
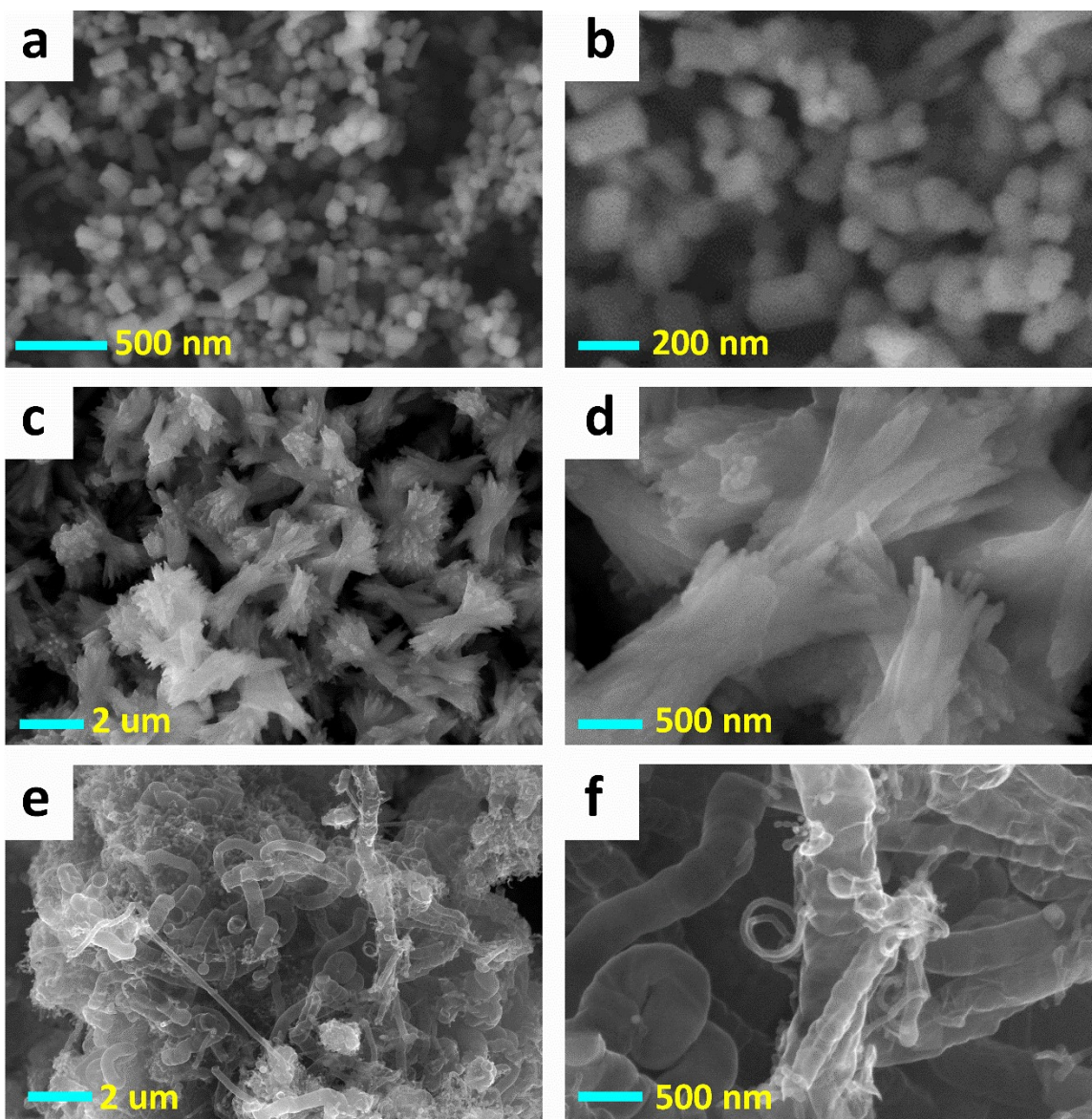
Fig. S5 SEM images of (a,b) ZnFeCu-MOF-74 seeds, (c,d) ZnFeCu-MOF-74 nanorod bundles, and (e,f) FeCu-DSAs@CNT at different magnifications.
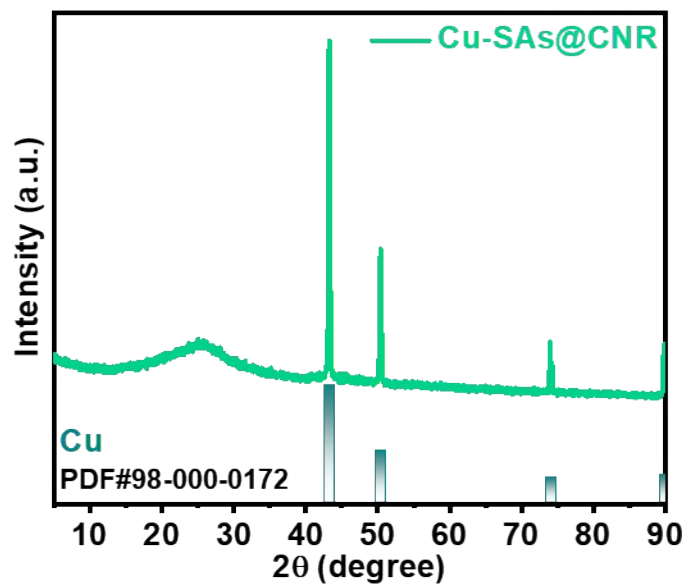
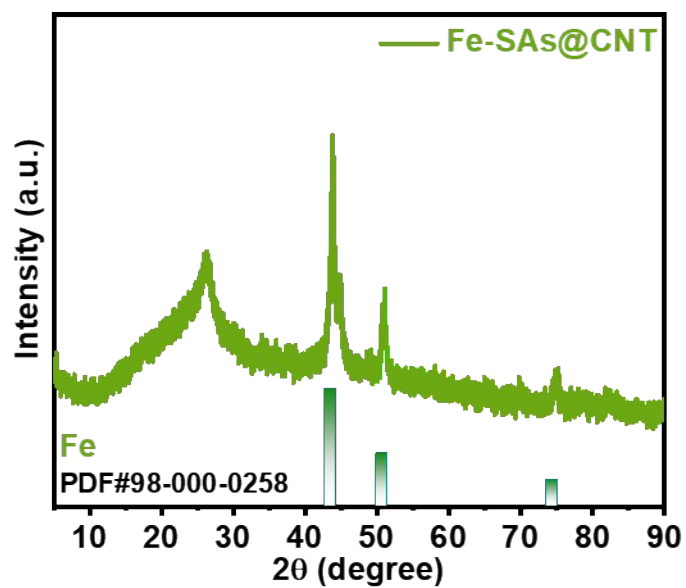**Fig. S6** Powder XRD patterns of Cu-SAs@CNR.
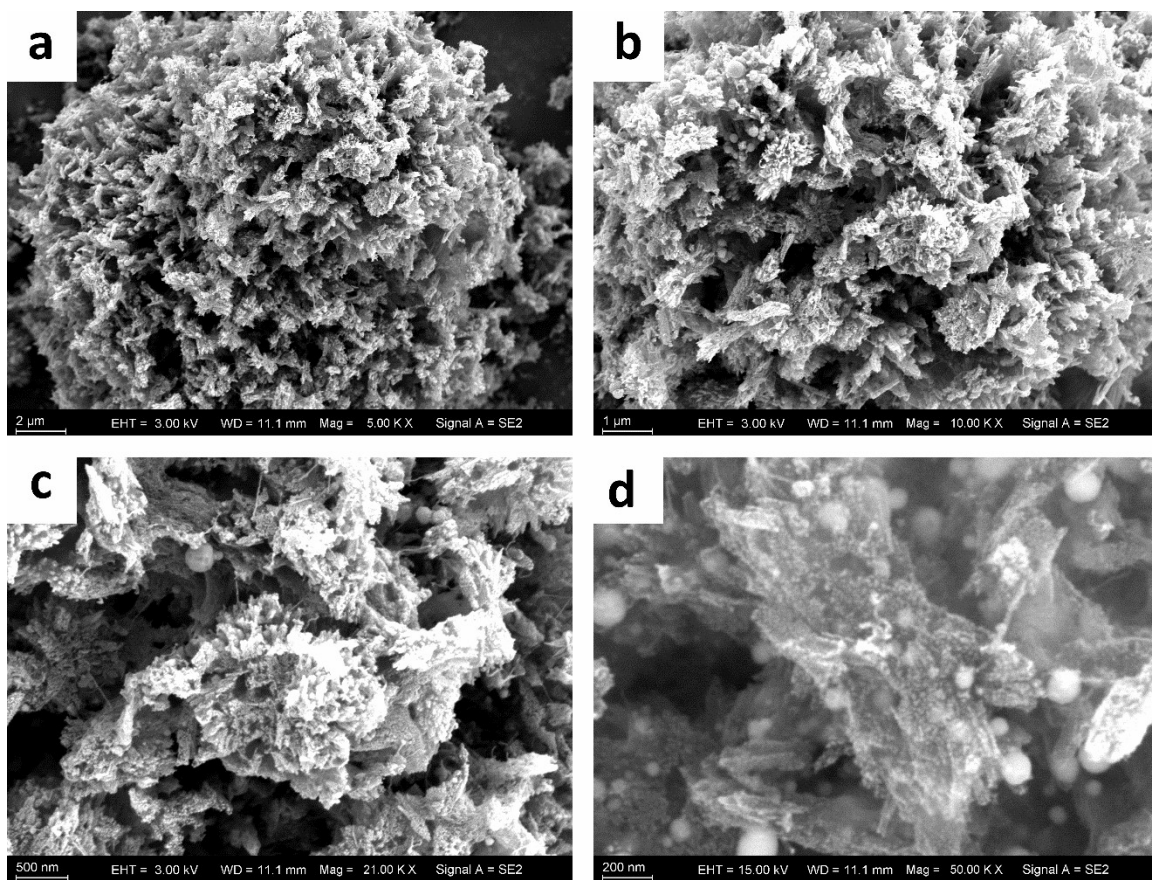

Fig. S7 Powder XRD patterns of Fe-SAs@CNT.

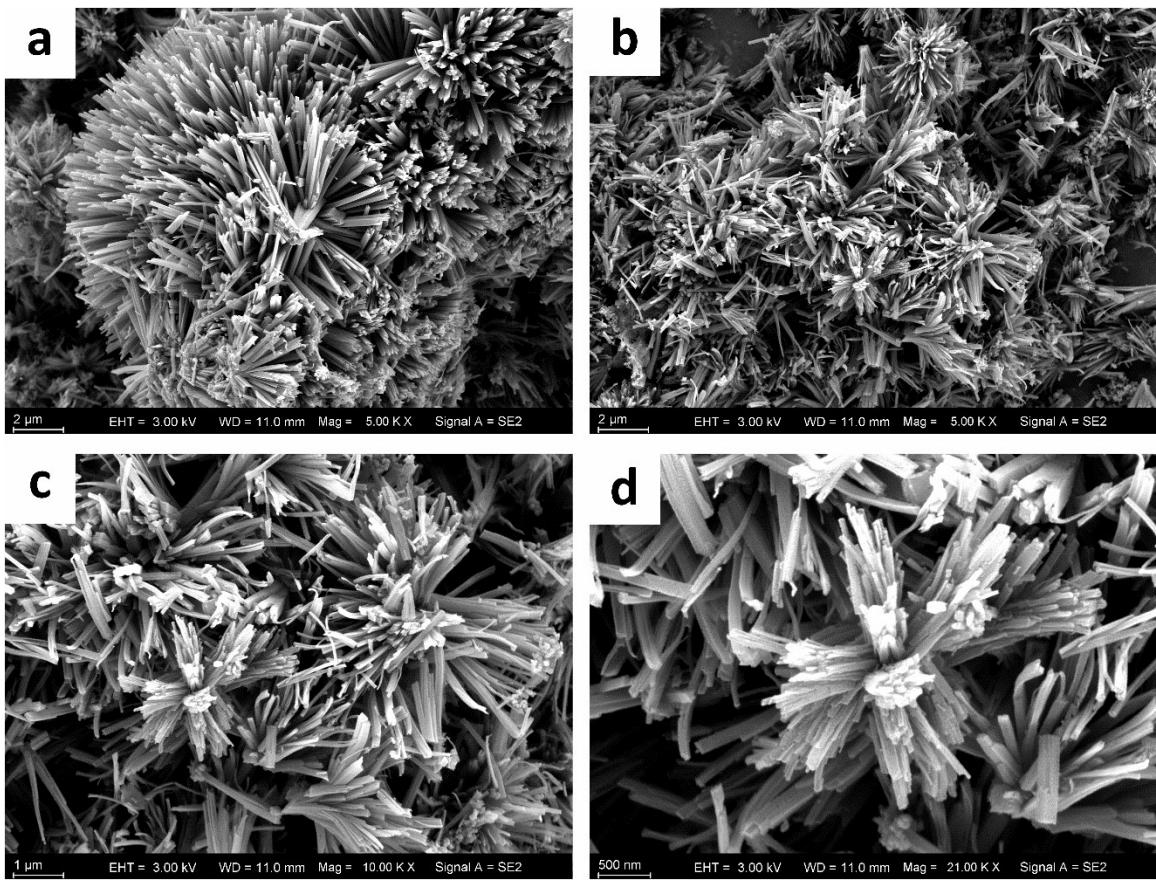**Fig. S8** (a-d) SEM images of FeCu-NPs@CNR at different magnifications.

Fig. S9 (a-d) SEM images of C@900 at different magnifications.
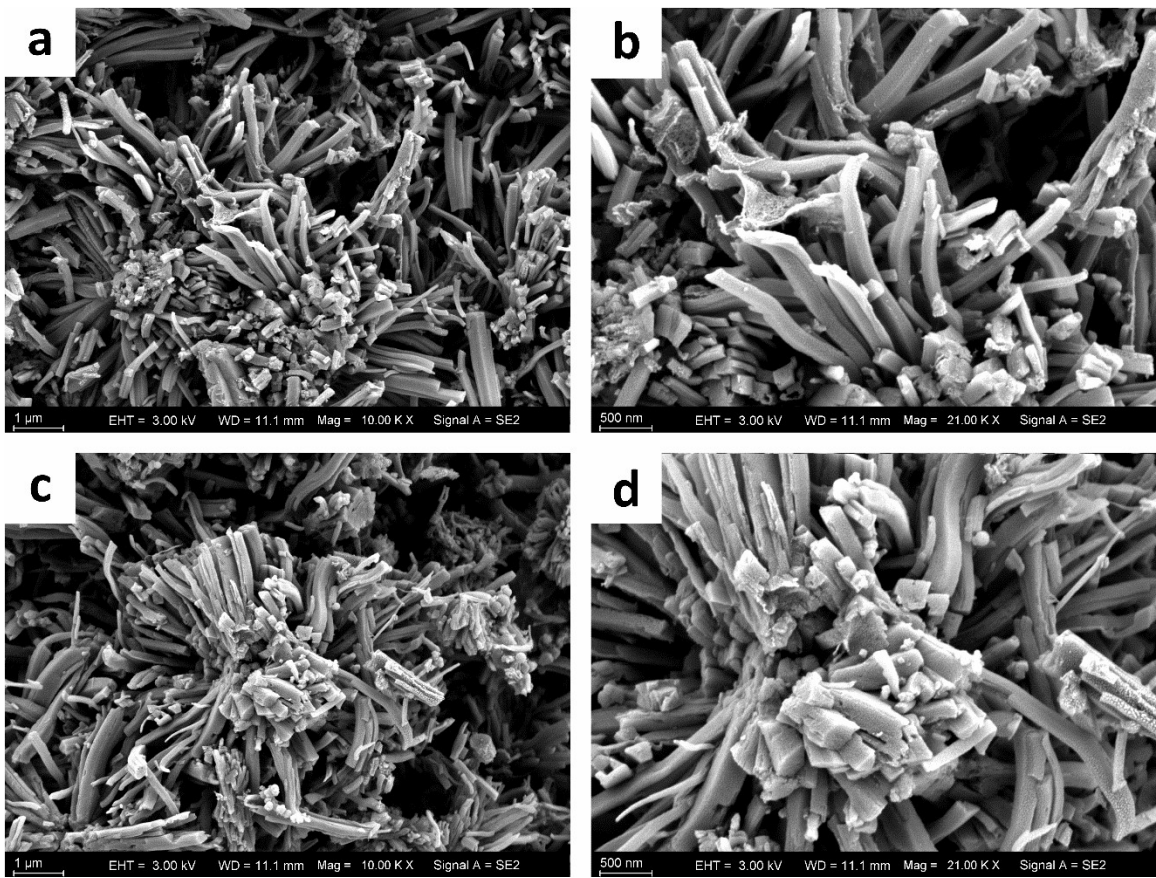
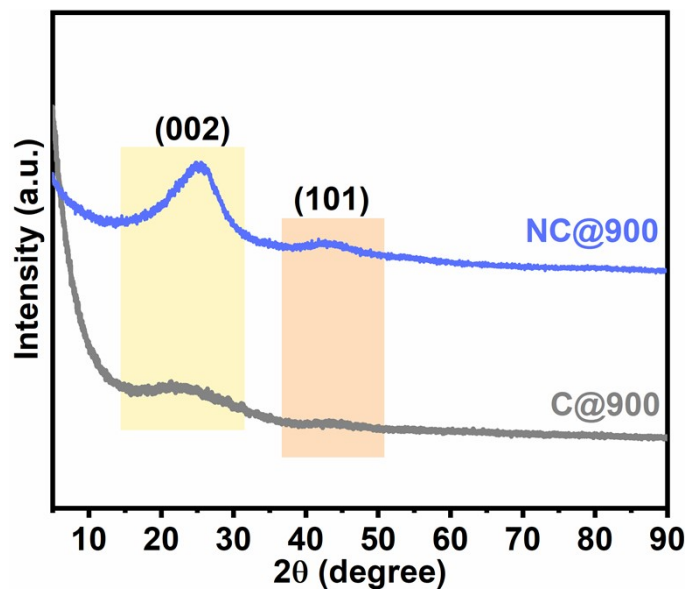**Fig. S10** (a-d) SEM images of NC@900 at different magnifications.

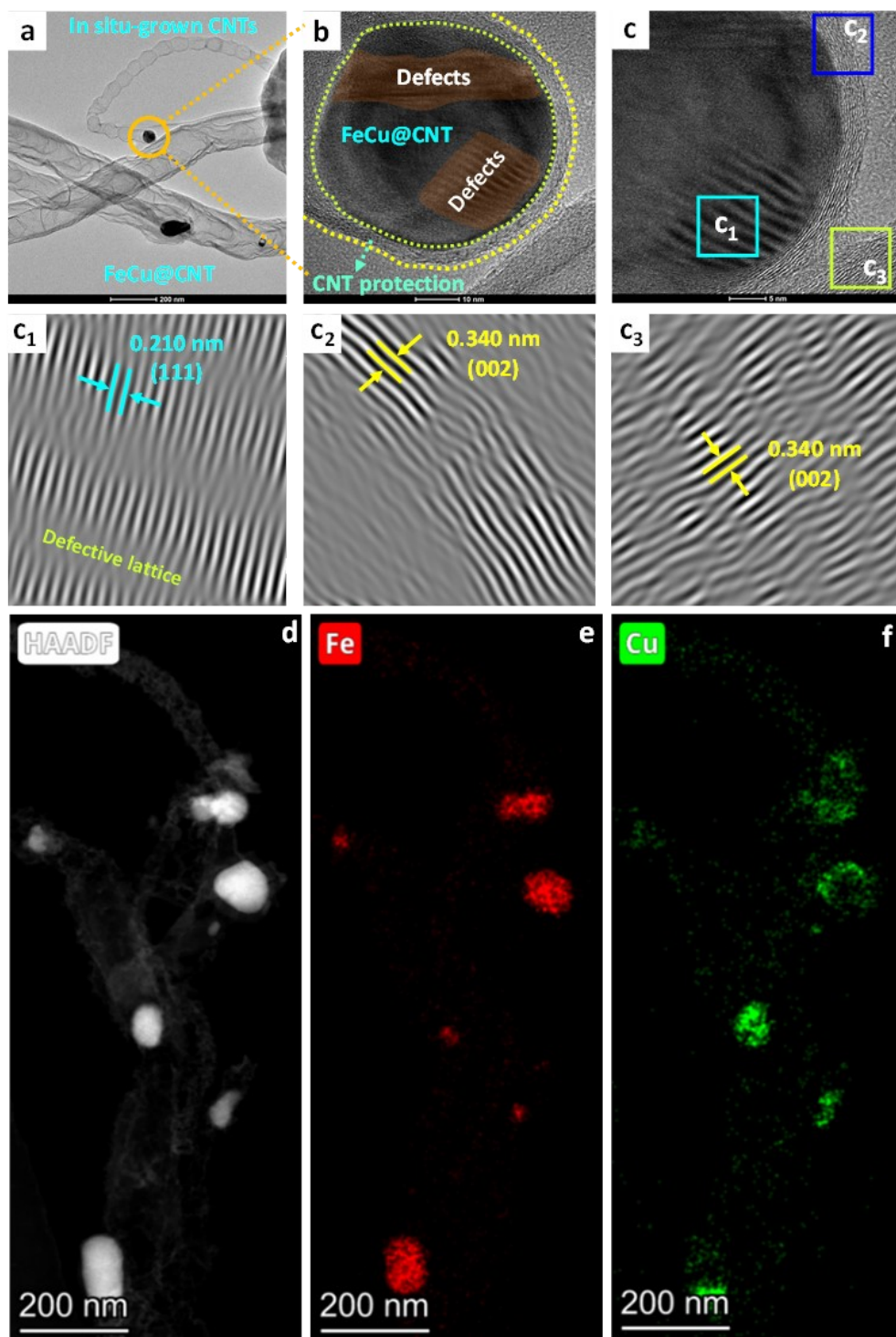**Fig. S11** Powder XRD patterns of C@900 and NC@900.

Fig. S12 (a-c) TEM and HR-TEM images of FeCu-DSAs@CNT, and C_1-C_3 are the zoomed-in view of different locations in Fig. C, and (d-f) HAADF-STEM and the corresponding EDS-mapping images of Fe and Cu elements.
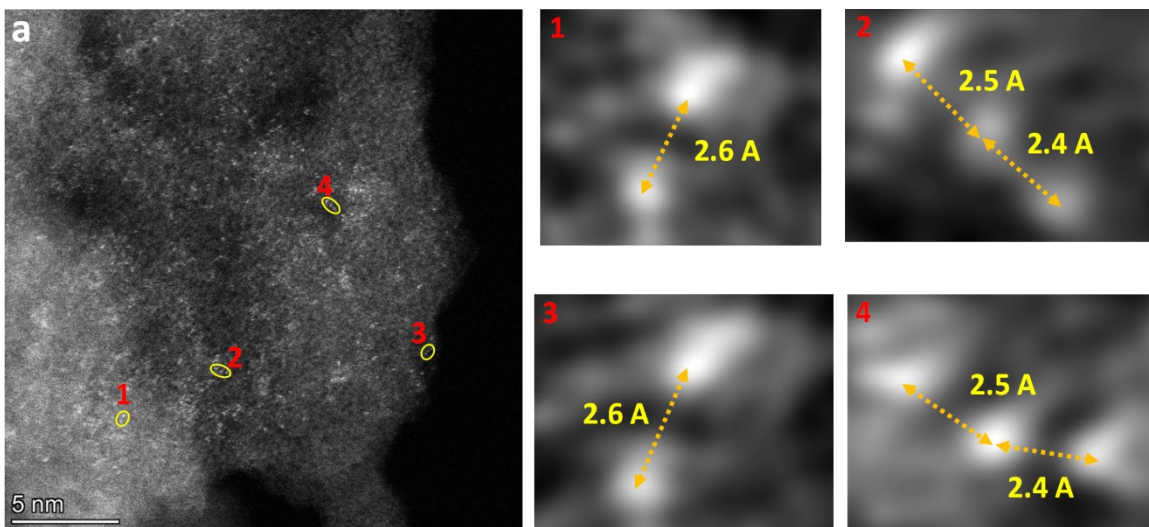
Fig. S13 AC-HAADF-STEM and the distance between atomically dispersed sites in FeCu-DSAs@CNT.[4–6]
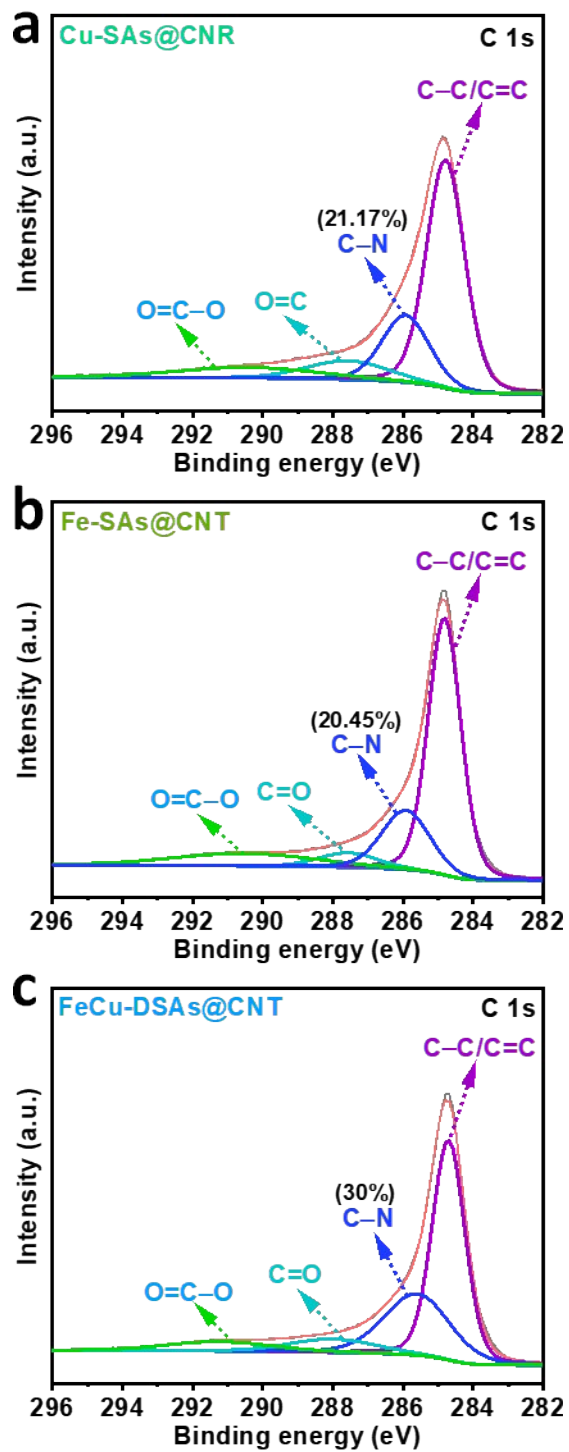
Fig. S14 (a-c) C 1s XPS spectral data of Cu-SAs@CNR, Fe-SAs@CNT, and FeCu-DSAs@CNT, respectively.
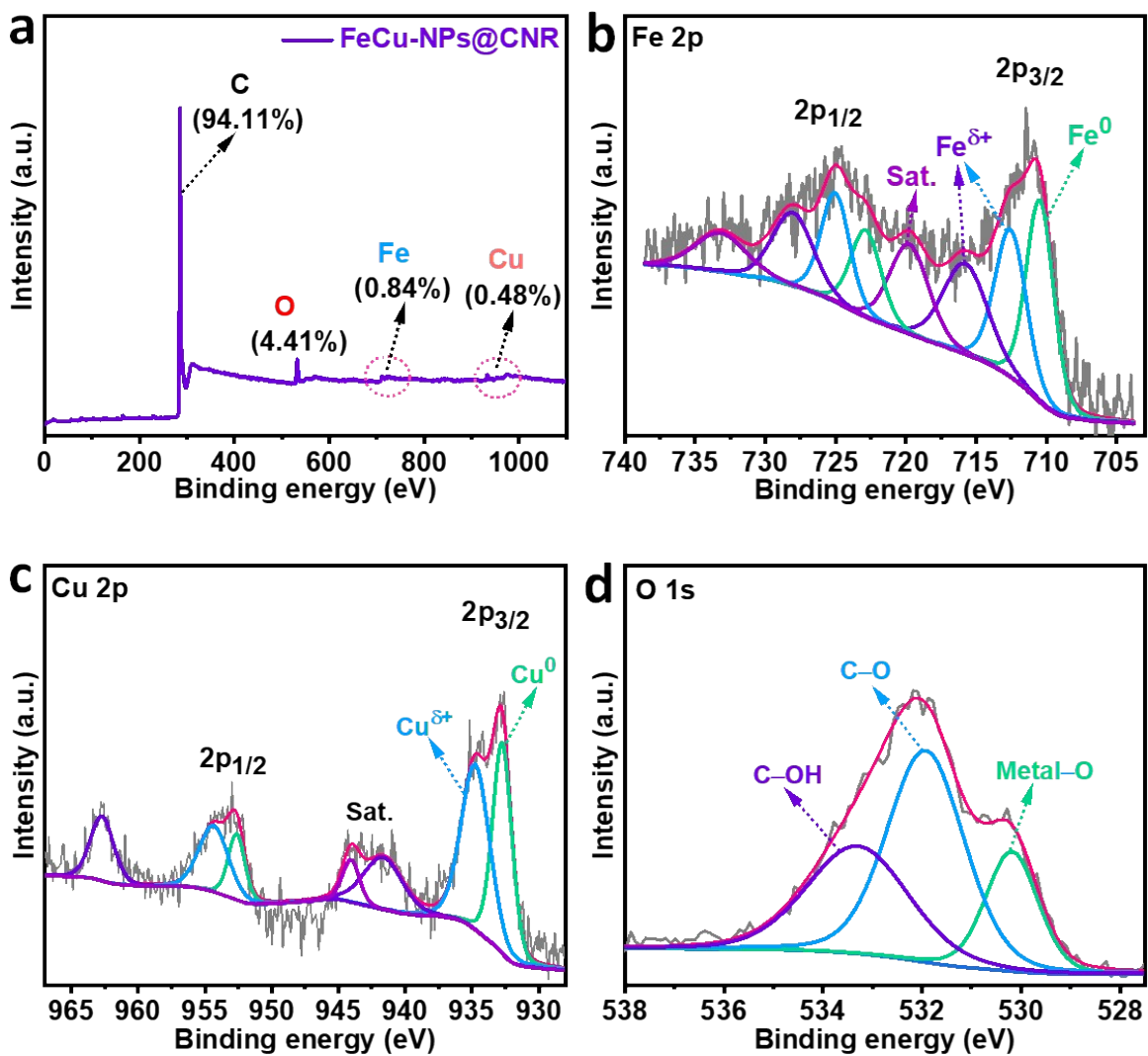
Fig. S15 (a) XPS survey spectrum, (b) Fe 2p, (c) Cu 2p and (d) O 1s XPS spectral data of FeCu-NPs@CNR, respectively (**Note:** The Fe$^{\delta+}$ and Cu$^{\delta+}$ peaks represent the surface oxidized peaks, instead of M-N$_x$ peaks as there was no nitrogen-incorporation).[7]

Fig. S16 (a-e) SEM-based EDS-mapping images and the corresponding elemental content of FeCu-NPs@CNR (inset shows the average elemental content of two tests data).
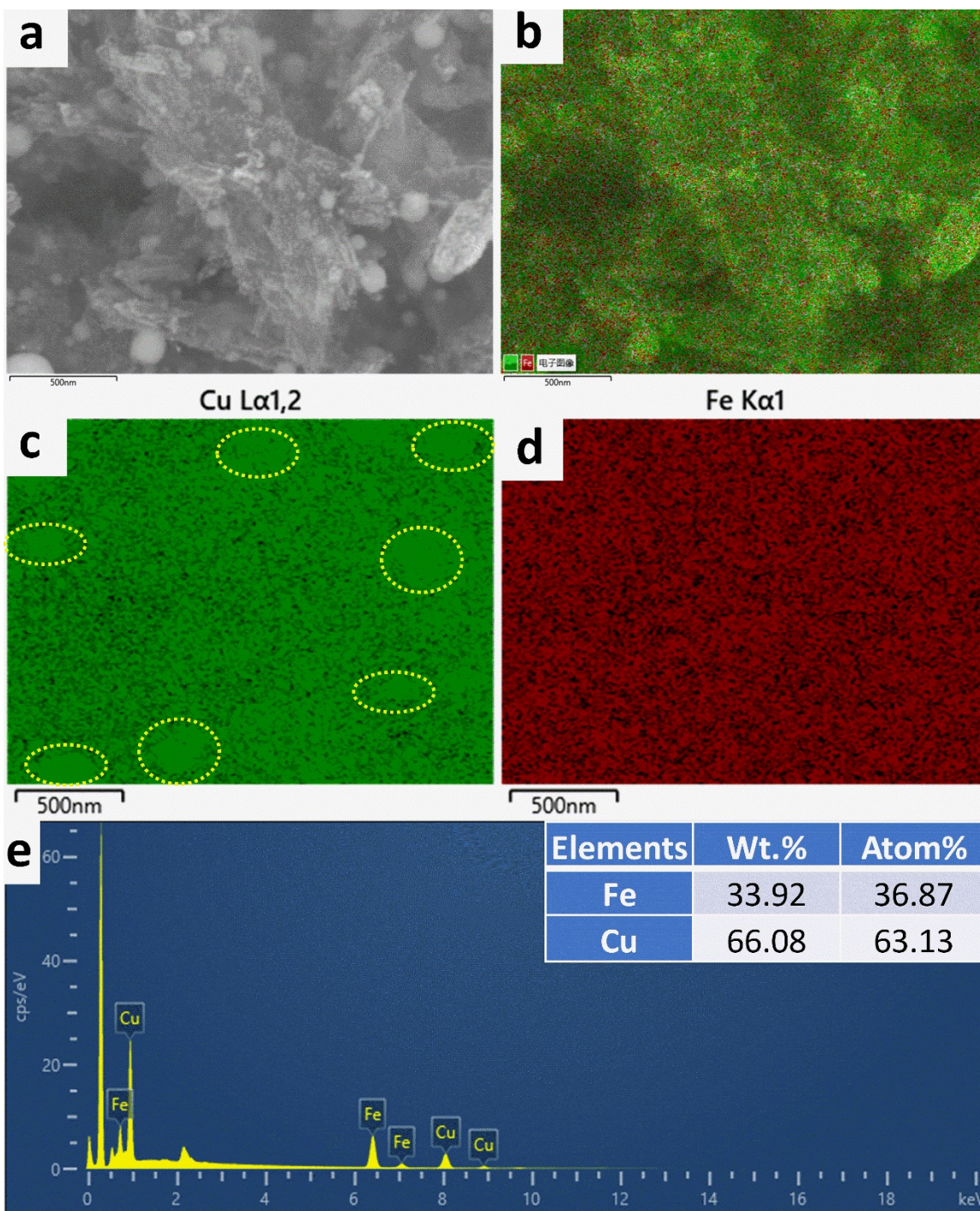
Fig. S17 (a-e) SEM-based EDS-mapping images and the corresponding elemental content of FeCu-DSAs@CNT (inset shows the average elemental content of two tests data).

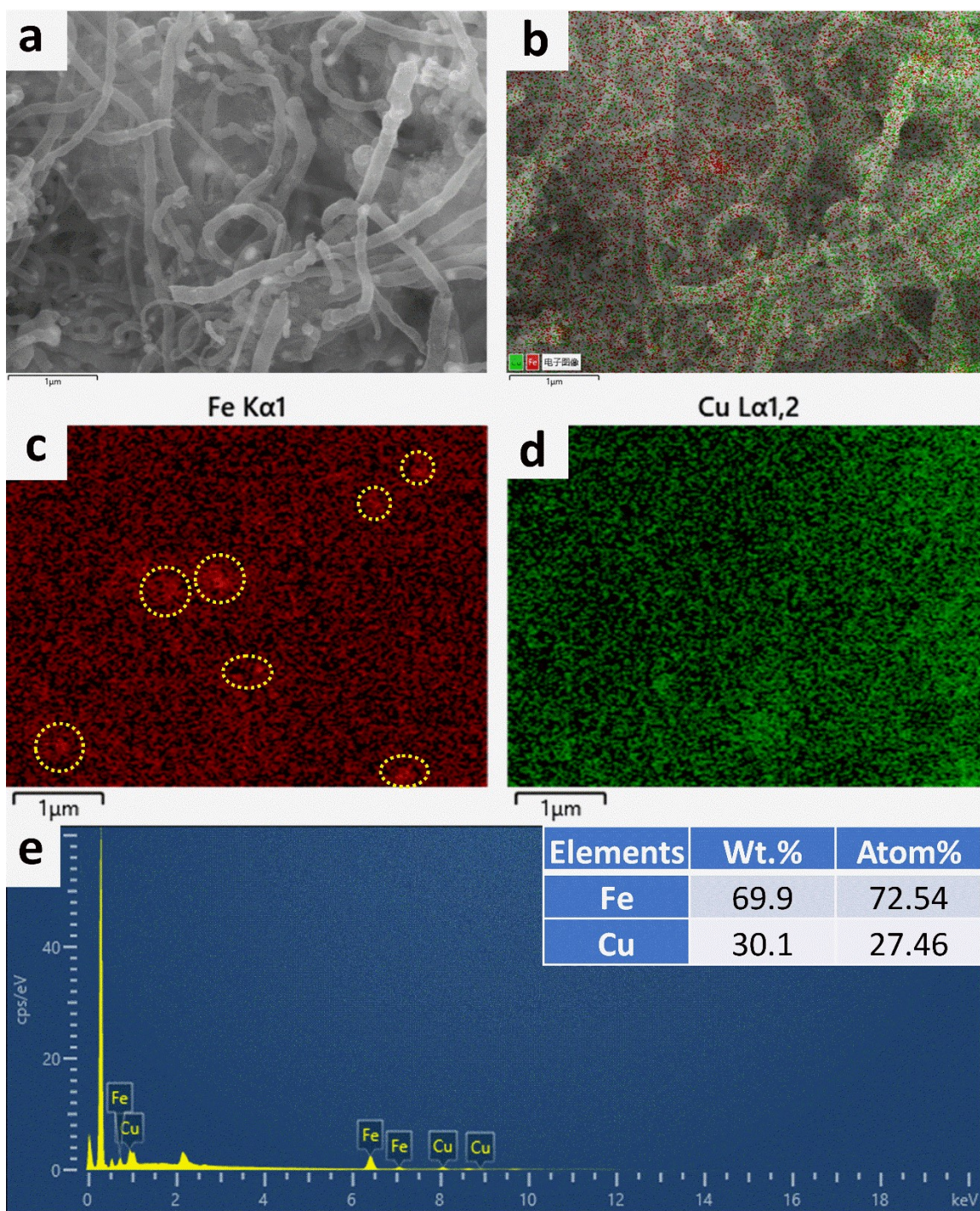**Fig. S18** (a-d) SEM images of FeCu-DSAs@CNT-AW at different locations and magnifications.
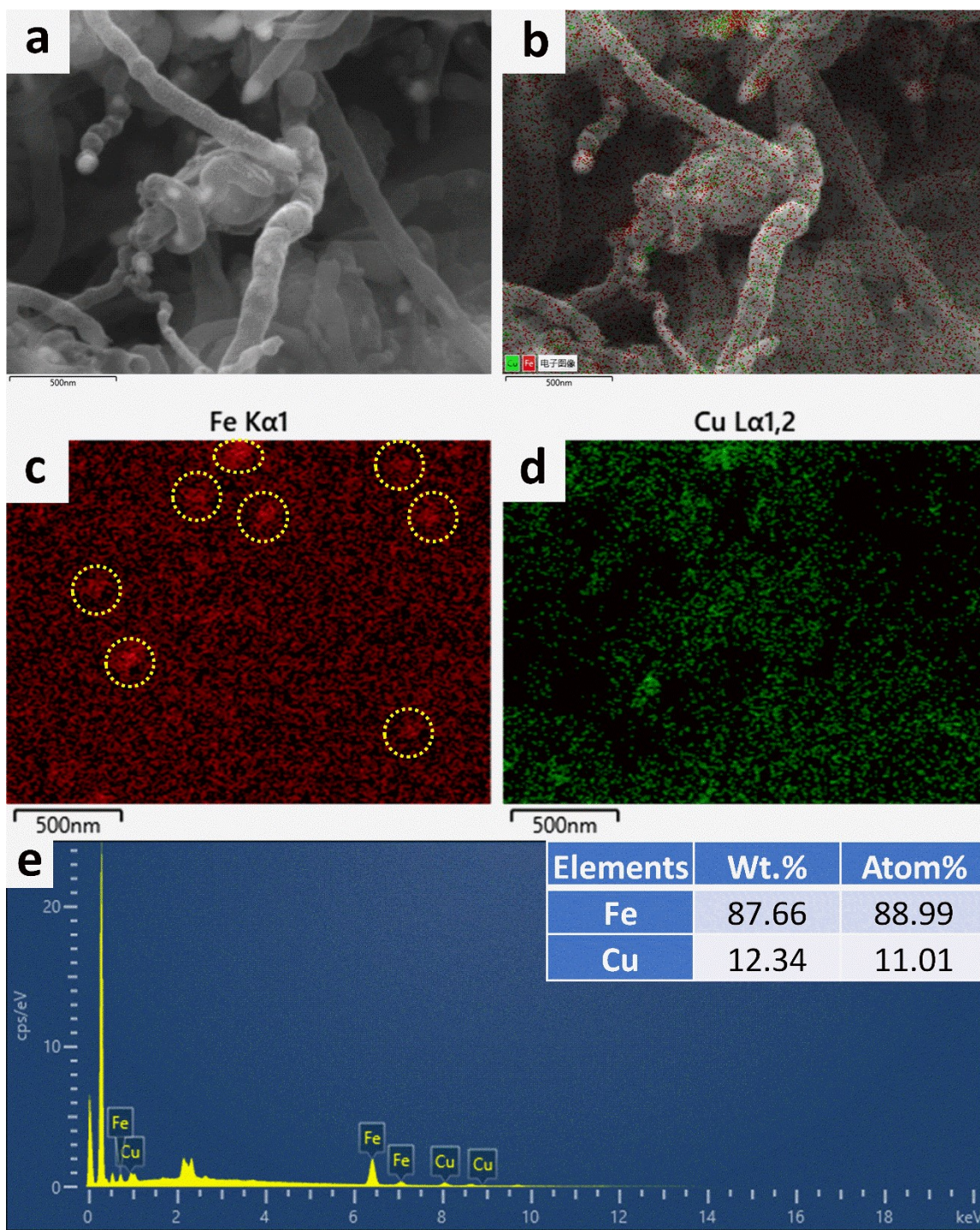
Fig. S19 (a-e) SEM-based EDS-mapping images and the corresponding elemental content of FeCu-DSAs@CNT-AW (inset shows the average elemental content of two tests data).
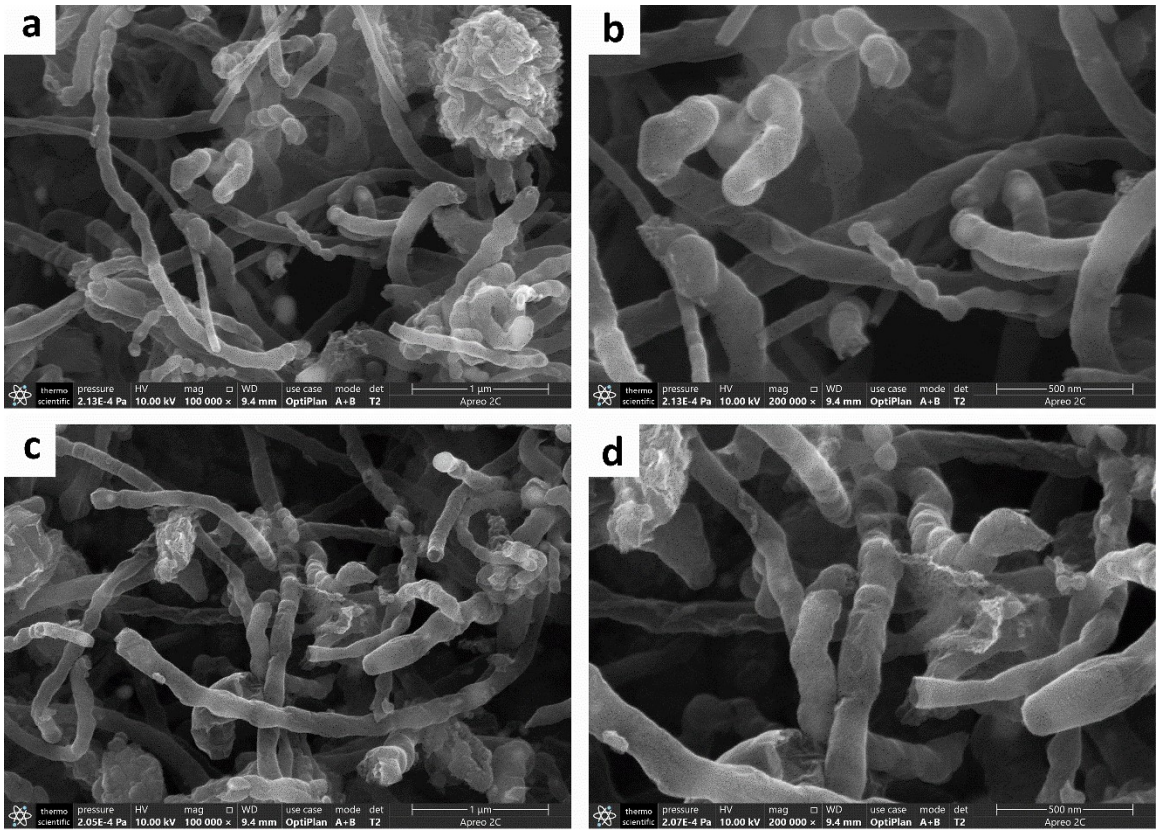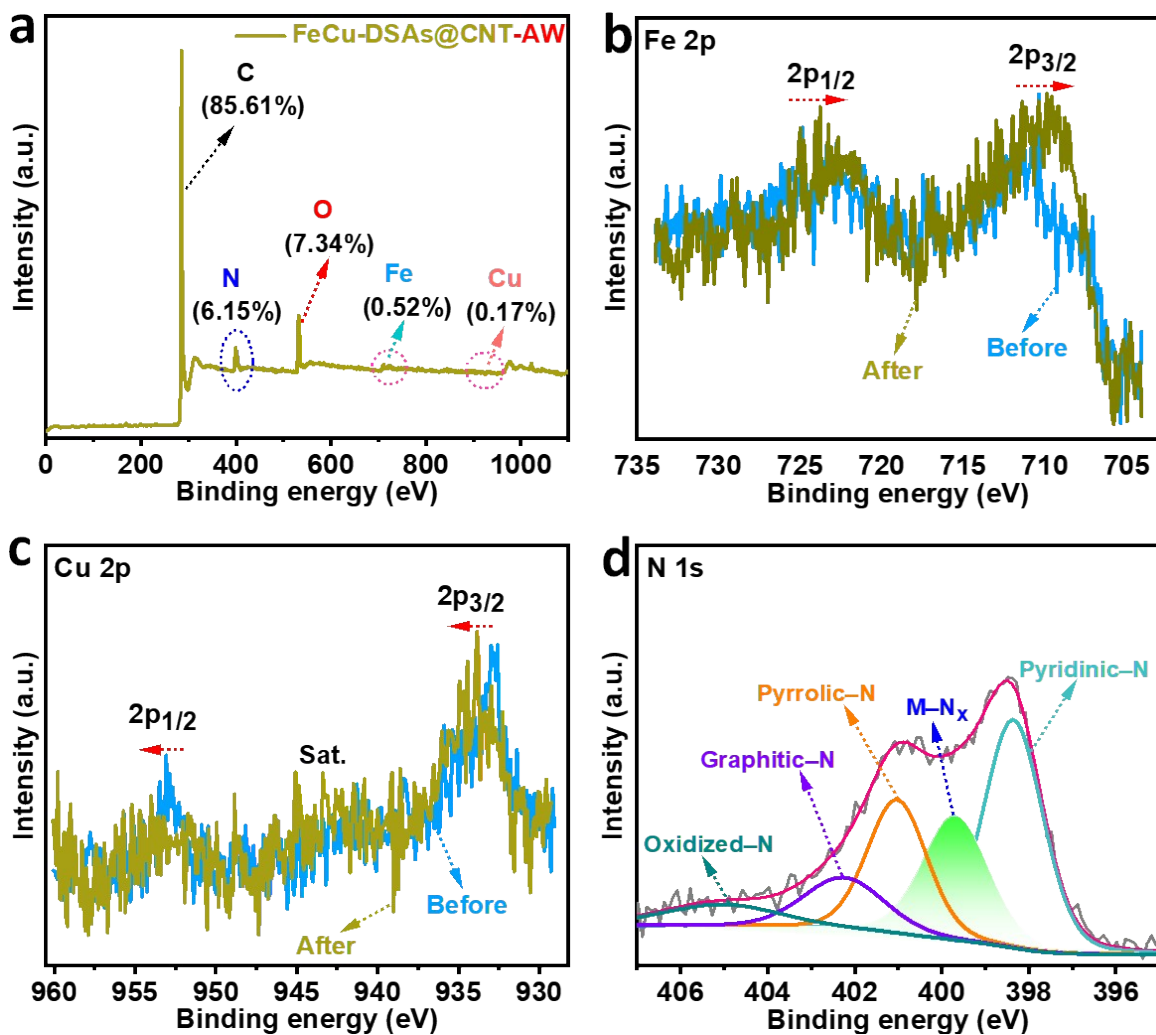
Fig. S20 (a) XPS survey spectrum, (b) Fe 2p, (c) Cu 2p and (d) N 1s XPS spectral data of FeCu-DSAs@CNT-AW, respectively.
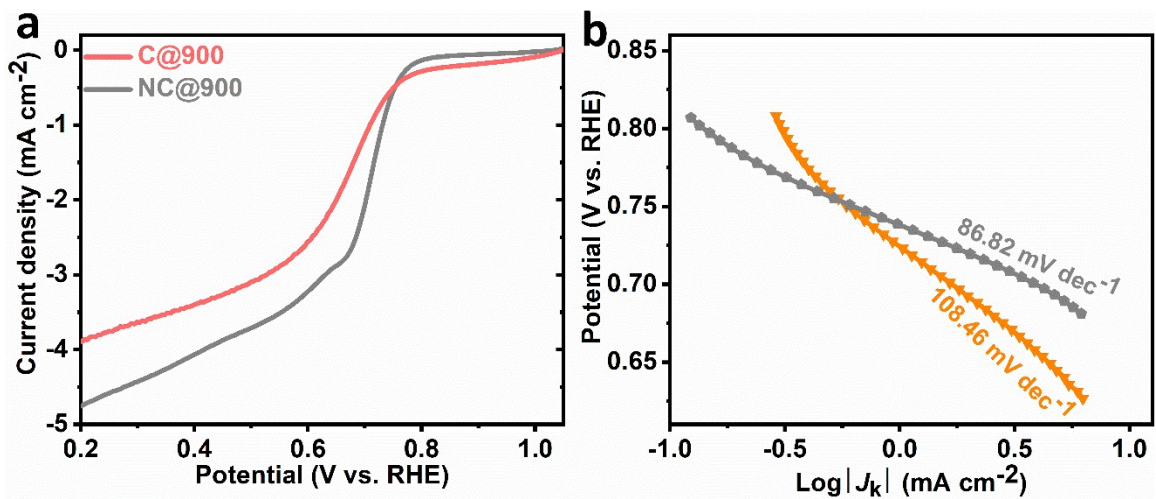
Fig. S21 (a,b) LSV curves and the corresponding Tafel slopes of C@900 and NC@900.
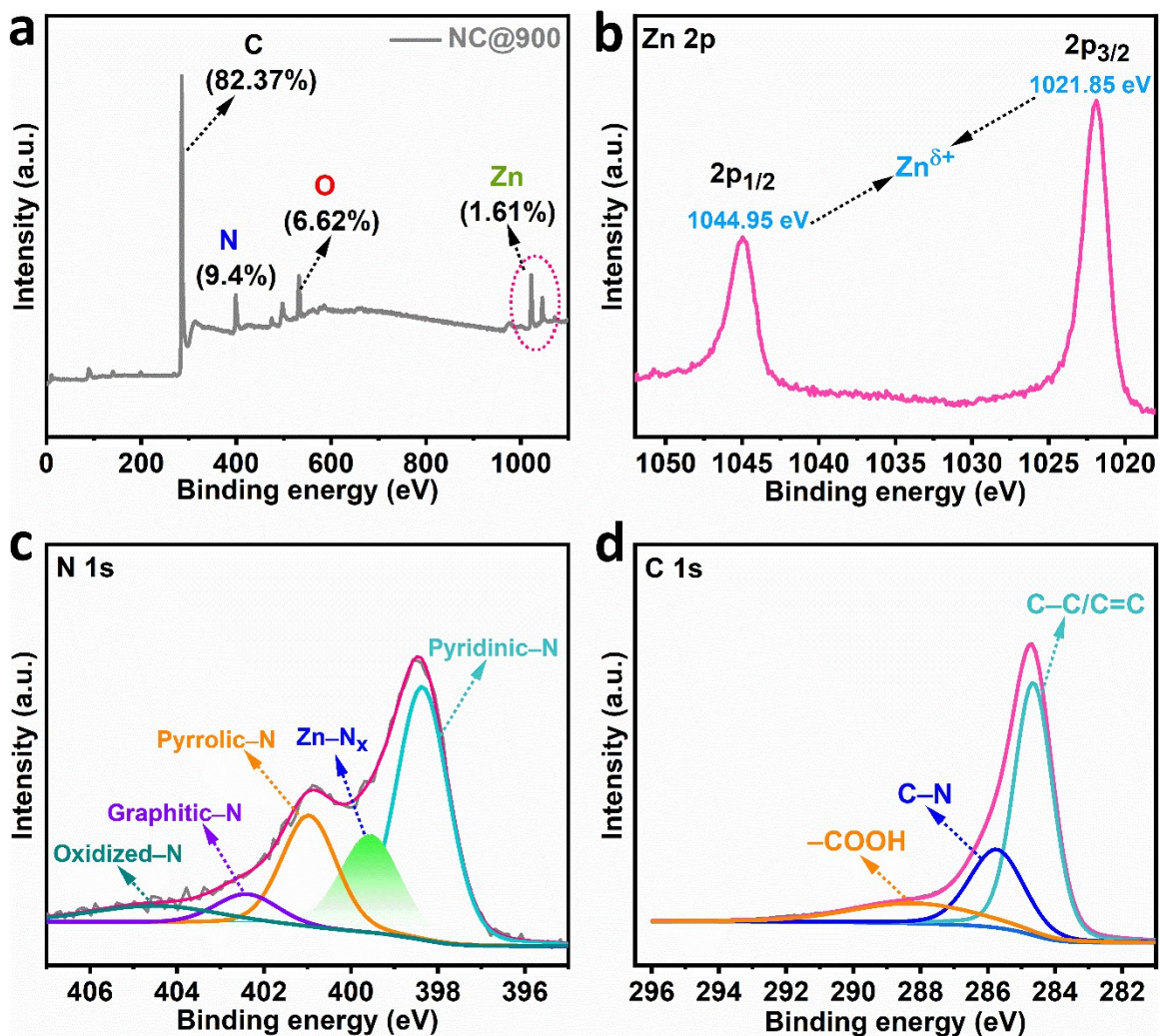
Fig. S22 (a) XPS survey spectrum, (b) Zn 2p, (c) N 1s, and (d) C 1s XPS spectral data of NC@900.
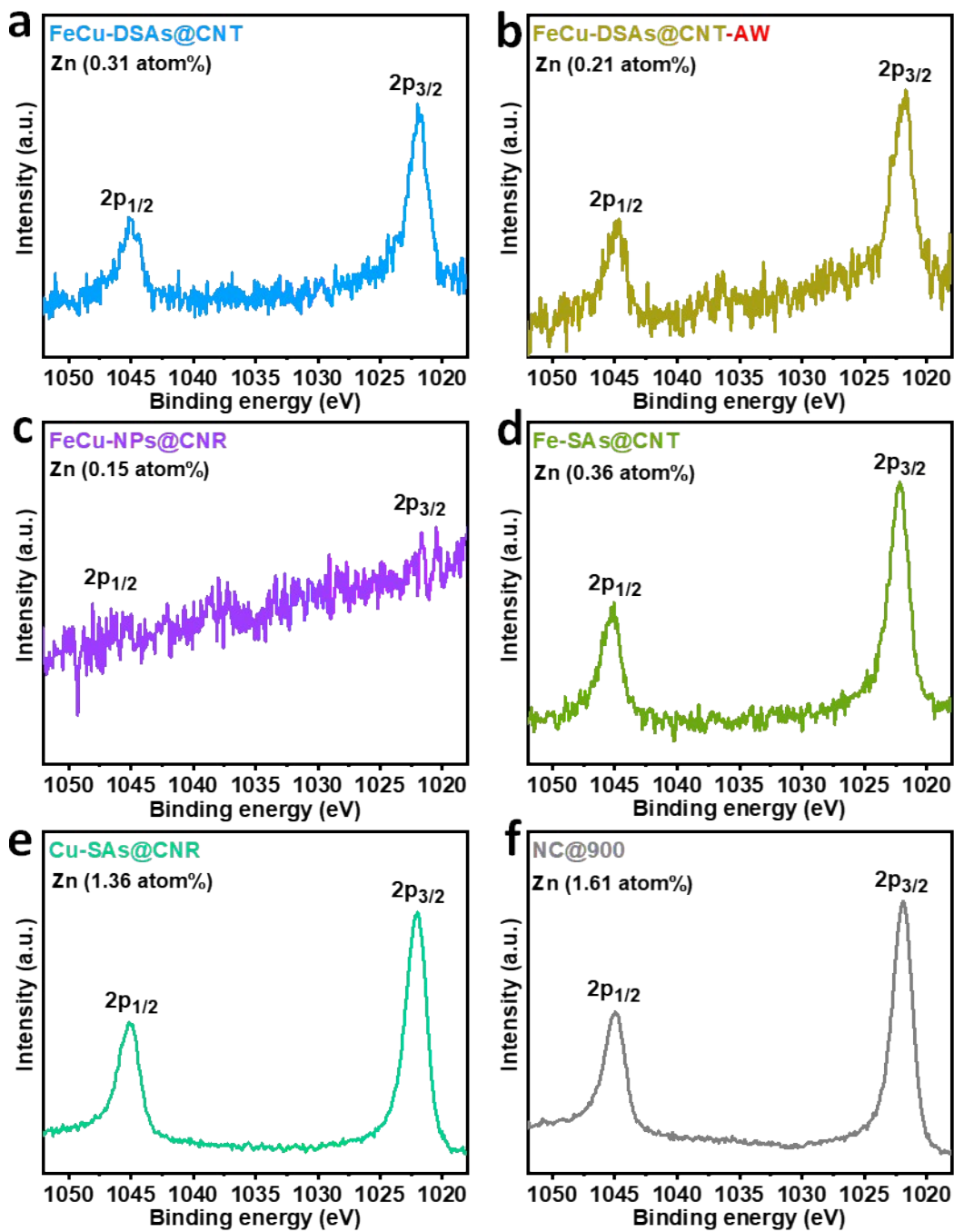
Fig. S23 Zn 2p XPS spectral data of (a) FeCu-DSAs@CNT, (b) FeCu-DSAs@CNT-AW, (c) FeCu-NPs@CNR, (d) Fe-SAs@CNT, (e) Cu-SAs@CNR and (f) NC@900, respectively.
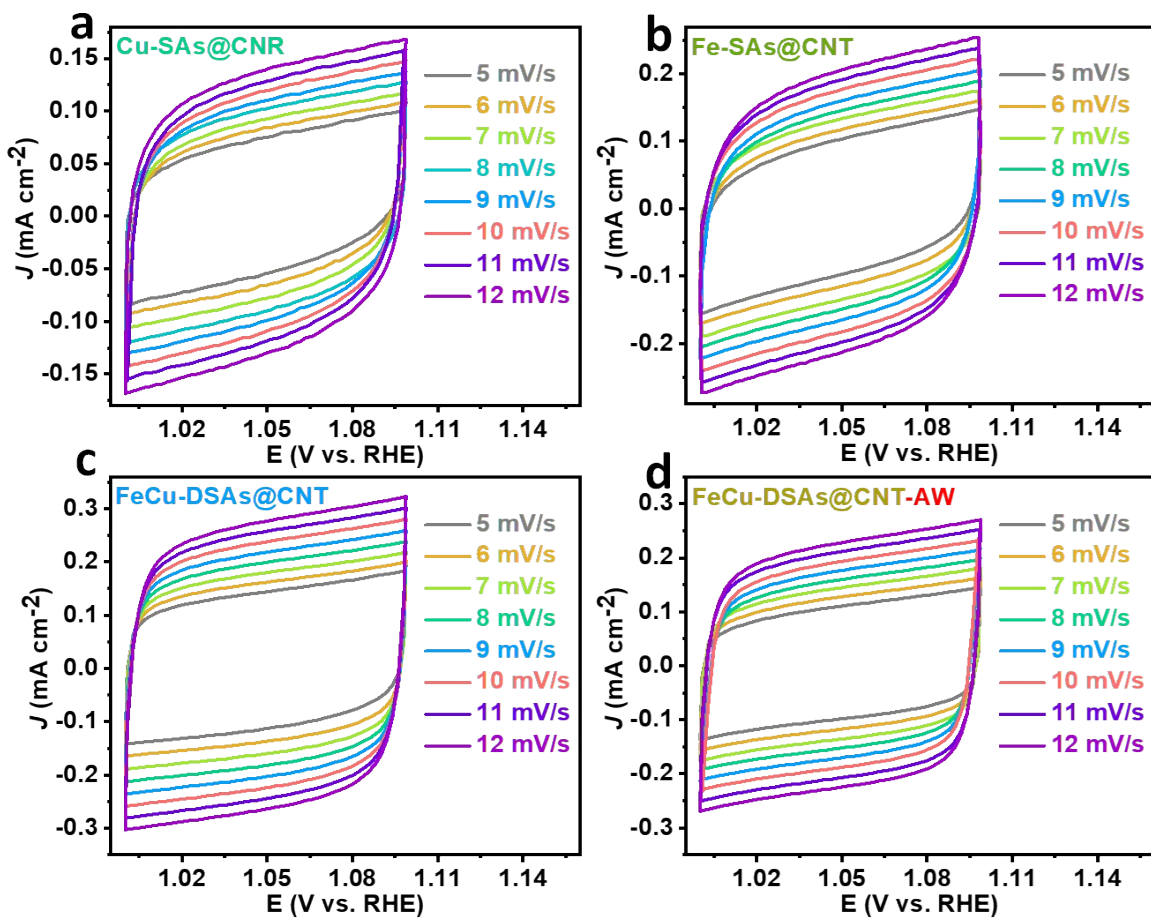
Fig. S24 (a-d) The plots of cyclic voltammograms operated within a non-Faradaic capacitive current range to estimate the ECSA in 0.1 M KOH electrolyte.
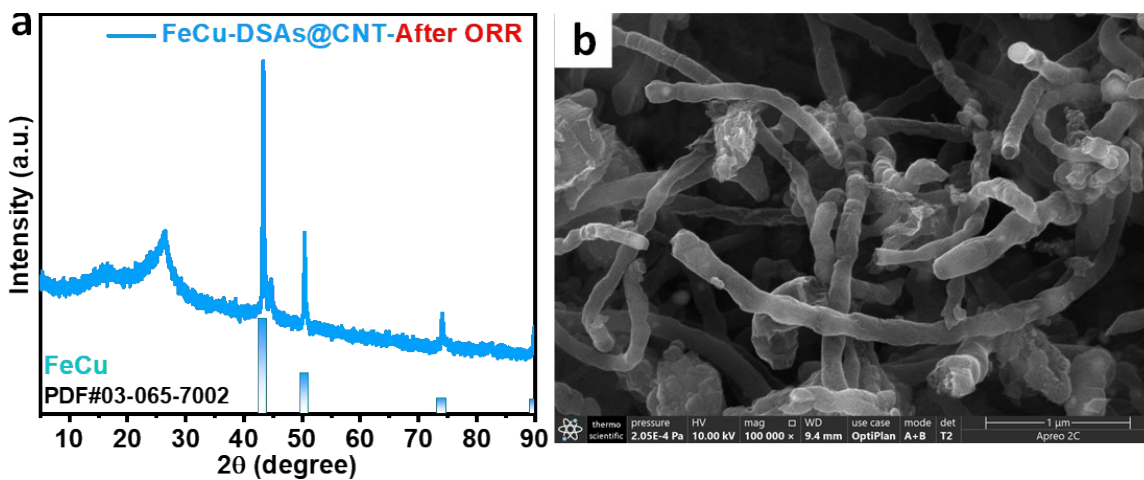
Fig. S25 (a) Powder XRD data, and (b) the SEM image of FeCu-DSAs@CNT-after ORR.
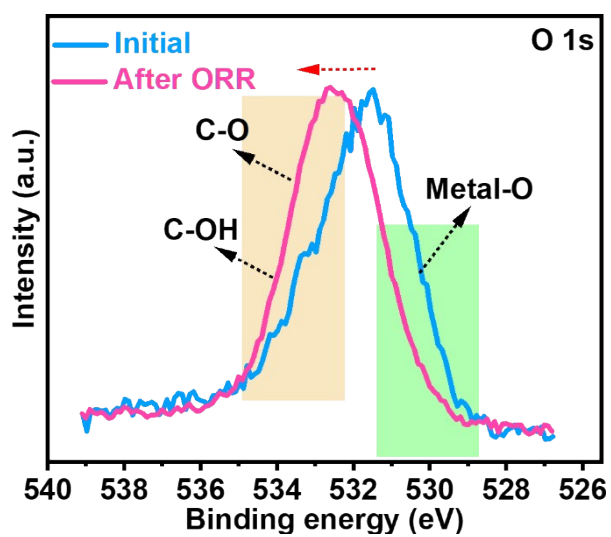
Fig. S26 O 1s XPS spectral data of FeCu-DSAs@CNT-after ORR, in comparison to its initial data.
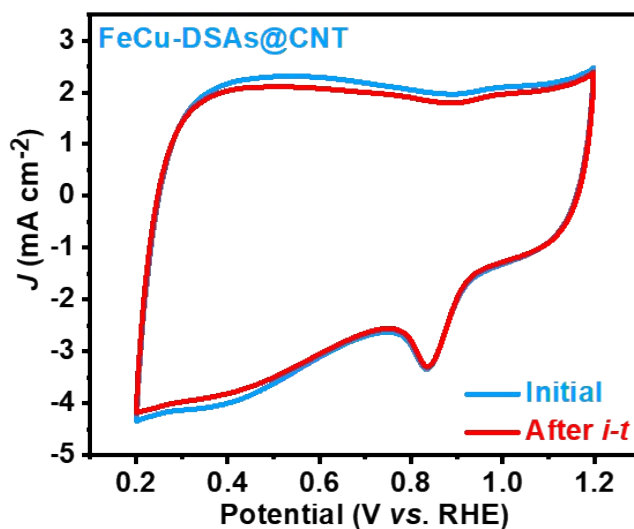
Fig. S27 CV plots obtained before and after OER *i-t* for FeCu-DSAs@CNT.
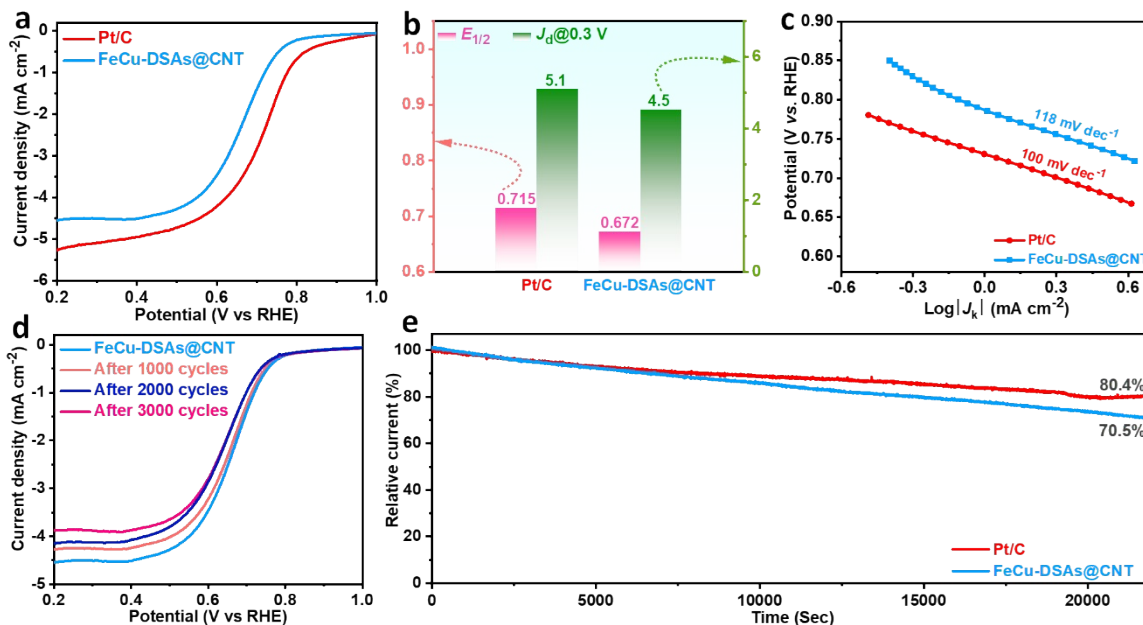
Fig. S28 (a) LSV plots, (b) the corresponding $E_{1/2}$ and J_d data, and (c) the Tafel slopes of Pt/C and FeCu-DSAs@CNT electrocatalysts in 0.5 M H_2SO_4 electrolyte. (d) Initial LSV curve of FeCu-DSAs@CNT in association with LSV curves obtained after ORR CV cycling tests, and (e) the long-term *i-t* plots of both FeCu-DSAs@CNT and Pt/C in 0.5 M H_2SO_4.
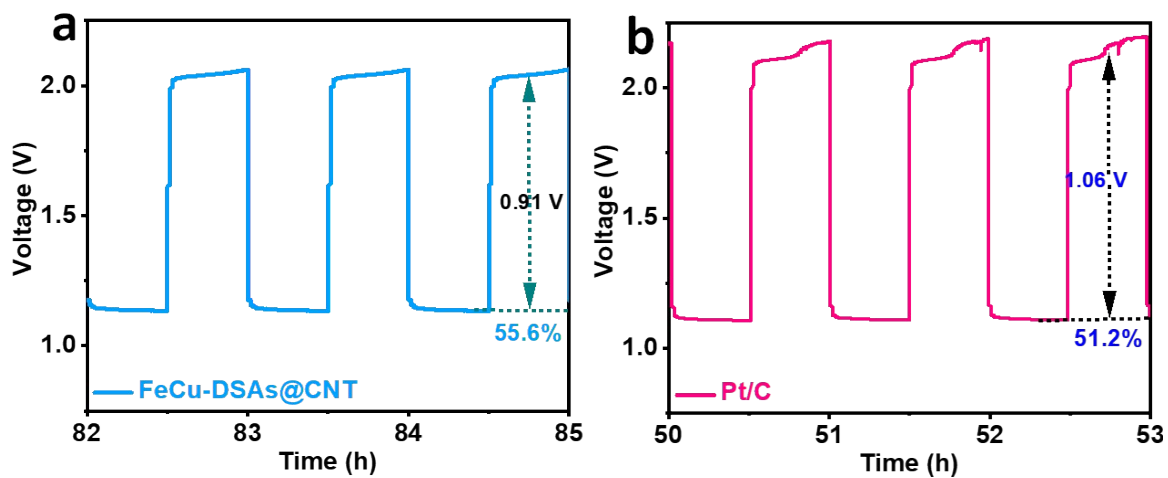
Fig. S29 Zoomed-in views of chare/discharge plots of (a) FeCu-DSAs@CNT and (b) Pt/C-based batteries at the end of the respective experiments.

Table S1: ORR performance of FeCu-DSAs@CNT in comparison with the other **dual single-atom site catalysts** reported recently in 0.1 M KOH solution.

Materials	E_{onset} (V)	$E_{1/2}$ (V)	J_d at 0.3 V (mA cm^{-2})	Ref.
FeCu-DSAs@CNT	**1.06**	**0.91**	**6.05**	
Fe-SAs@CNT	**1.0**	**0.852**	**4.35**	**This work**
Cu-SAs@CNR	**0.972**	**0.786**	**4.16**	
Pt/C (20 wt.%)	**0.975**	**0.847**	**5.38**	
FeCu-NC	0.96	0.882	~5.7	
Fe-NC	0.93	0.858	~5.5	[8]
Cu-NC	0.89	0.825	~5.2	
Pt/C	0.92	0.843	~5.5	
Fe/Cu-N-C	1.007	0.879	~5.9	
Fe-N-C	0.968	0.861	~5.8	[9]
Cu-N-C	0.905	0.798	~5.9	
Pt/C	0.972	0.835	~5.3	
NCAG/Fe-Cu	1.07	0.94	~5.9	
NCAG/Fe-Fe	1.04	0.90	~5.8	[10]
Pt/C	0.99	0.86	~5.3	
Fe,Cu DAs-NC	1.08	0.94	~6.0	
Fe SA-NC	1.05	0.92	~5.6	[11]
Cu SA-NC	1.00	0.84	~5.0	

Pt/C	1.04	0.87	~5.5	
FeCo-N-HCN	0.98	0.86	~5.6	
Fe-N-HCN	0.96	0.76	~5.3	12
Pt/C	1.03	0.85	~5.8	
FeCu-NC	0.98	0.87	~5.9	13
FeCu-SAC	NA	0.926	~5.8	
Fe-SAC	NA	0.899	~5.6	
Cu-SAC	NA	0.810	~4.6	14
Pt/C	NA	0.884	~5.8	
Fe-Cu-N/C	NA	0.89	~5.8	15
Pt/C	NA	0.84	~5.4	
FeCu-DA/NC	0.96	0.86	~6.0	
Fe-DA/NC	0.91	0.8	~6.0	
Cu-DA/NC	0.87	0.78	~5.0	16
Pt/C	0.94	0.83	~5.5	

Abbreviations: NA = not available; NCAG = nitrogen-doped carbon aerogel; N-HCN = N-doped hollow carbon nanocages; SA = Single-atom; DA = Dual-atom, and NC = N-doped carbon.

Table S2: ORR performance of FeCu-DSAs@CNT in comparison with **other nanoparticles coupled SACs or DSACs** reported recently.

Materials	Atomic sites	Associated particle	$E_{1/2}$ (V)	Tafel slope (mV dec^{-1})	Ref.
FeCu-DSAs@CNT	**Fe-N$_x$ & Cu-N$_x$**	**FeCu**	**0.91**	**48.15**	**This work**
Cu@Fe-N-C	Fe-N$_x$ & Cu-N$_x$	Cu	0.892	65	[17]
Cu/Fe-NG	Fe-N$_x$ & Cu-N$_x$	Cu	0.88	74	[18]
Fe–Ni ANC@NSCA	Fe-N$_4$ & Ni-N$_4$	Fe-Ni	0.891	63	[19]
FePc‖CNTs‖NiCo/CP	Fe-N$_4$	NiCo	0.902	50	[20]
Fe$_x$/Cu–N@CF	Cu-N$_4$	Fe$_x$	0.944	52.61	[21]
Fe-N-HMCTs	Fe-N$_x$	Fe$_3$C	0.872	89	[22]
1MIL/40ZIF-1000	Fe-N$_x$	Fe-Fe$_3$C	0.88	50	[23]
Fe$_3$C@NCNTs	Fe-N$_x$	Fe$_3$C	0.84	77	[24]
NP-Fe-NHPC	Fe-N$_x$	Fe$_3$C	0.88	NA	[25]

Abbreviations: NG = N-doped graphene; ANC@NSCA = alloy nanoclusters (Fe–Ni ANCs) anchored on N, S co-doped carbon aerogel; CF = carbon nanofiber; N-HMCTs = N-doped hollow mesoporous carbon tubes; NCNTs = N-doped carbon nanotubes; NHPC = hierarchically porous carbon.

References:

1   G. Kresse and J. Hafner, *Phys. Rev. B*, 1994, **49**, 14251–14269.

2   L. Yu, X. Pan, X. Cao, P. Hu and X. Bao, *J. Catal.*, 2011, **282**, 183–190.

3   S. Zuluaga and S. Stolbov, *J. Chem. Phys.*, 2011, **135**, 134702.

4   C. Brea and G. Hu, *ACS Catal.*, 2023, **13**, 4992–4999.

5   P. Li, F. Qiang, X. Tan, Z. Li, J. Shi, S. Liu, M. Huang, J. Chen, W. Tian, J. Wu, W. Hu and H. Wang, *Appl. Catal. B Environ.*, 2024, **340**, 123231.

6   H. Liu, L. Jiang, Y. Wang, X. Wang, J. Khan, Y. Zhu, J. Xiao, L. Li and L. Han, *Chem. Eng. J.*, 2023, **452**, 138938.

7   Y. Liu, J. Ma, S. Huang, S. Niu and S. Gao, *Nano Energy*, 2023, **117**, 108840.

8   Z. Xiao, P. Sun, Z. Qiao, K. Qiao, H. Xu, S. Wang and D. Cao, *Chem. Eng. J.*, 2022, **446**, 137112.

9   M. Bu, Y. Liu, S. Liao, W. Liu, Z. Yang, J. Jiang, X. Gao, Y. Yang and H. Liu, *Carbon N. Y.*, 2023, **214**, 118365.

10   T. He, Y. Chen, Q. Liu, B. Lu, X. Song, H. Liu, M. Liu, Y. Liu, Y. Zhang, X. Ouyang and S. Chen, *Angew. Chemie Int. Ed.*, 2022, **61**, e202201007.

11   F. Kong, M. Wang, Y. Huang, G. Meng, M. Chen, H. Tian, Y. Chen, C. Chen, Z. Chang, X. Cui and J. Shi, *Energy Storage Mater.*, 2023, **54**, 533–542.

12   H. Li, Y. Wen, M. Jiang, Y. Yao, H. Zhou, Z. Huang, J. Li, S. Jiao, Y. Kuang and S. Luo, *Adv. Funct. Mater.*, 2021, **31**, 2011289.

13   X. Zhou, K. Song, Y. Feng, C. Jiang, Z. Chen, Z. Wang, N. Yue, X. Ge, W. Zhang and W. Zheng, *Nano Res.*, 2023, **16**, 4634–4642.

14   H. Yang, H. Huang, Q. Wang, L. Shang, T. Zhang and S. Wang, *J. Mater. Chem. A*, 2023, **11**, 6191–6197.

15   W. Fan, Z. Li, C. You, X. Zong, X. Tian, S. Miao, T. Shu, C. Li and S. Liao, *Nano Energy*, 2017, **37**, 187–194.

16   C. Du, Y. Gao, H. Chen, P. Li, S. Zhu, J. Wang, Q. He and W. Chen, *J. Mater. Chem. A*, 2020, **8**, 16994–17001.

17   Z. Wang, H. Jin, T. Meng, K. Liao, W. Meng, J. Yang, D. He, Y. Xiong and S. Mu, *Adv. Funct. Mater.*, 2018, **28**, 1802596.

18   L. Xu, Y. Tian, D. Deng, H. Li, D. Zhang, J. Qian, S. Wang, J. Zhang, H. Li and S. Sun, *ACS Appl. Mater. Interfaces*, 2020, **12**, 31340–31350.

19   H. Li, X. Shu, P. Tong, J. Zhang, P. An, Z. Lv, H. Tian, J. Zhang and H. Xia, *Small*, 2021, **17**, 2102002.

20   S. Ding, L. He, L. Fang, Y. Zhu, T. Li, Z. Lyu, D. Du, Y. Lin and J. Li, *Adv. Energy Mater.*, 2022, **12**, 2202984.

21   S. Wu, S. Jiang, S.-Q. Liu, X. Tan, N. Chen, J.-L. Luo, S. H. Mushrif, K. Cadien and Z. Li, *Energy Environ. Sci.*, 2023, **16**, 3576–3586.

22   X. Cui, L. Gao, S. Lei, S. Liang, J. Zhang, C. D. Sewell, W. Xue, Q. Liu, Z. Lin and Y. Yang, *Adv. Funct. Mater.*, 2021, **31**, 2009197.

23   H. Wang, F. Yin, N. Liu, R. Kou, X. He, C. Sun, B. Chen, D. Liu and H. Yin, *Adv. Funct. Mater.*, 2019, **29**, 1901531.

24   C. Xu, C. Guo, J. Liu, B. Hu, J. Dai, M. Wang, R. Jin, Z. Luo, H. Li and C. Chen, *Energy Storage Mater.*, 2022, **51**, 149–158.

25   G. Chen, P. Liu, Z. Liao, F. Sun, Y. He, H. Zhong, T. Zhang, E. Zschech, M. Chen, G. Wu, J. Zhang and X. Feng, *Adv. Mater.*, 2020, **32**, 1907399.